Electronic Supporting Information

Phase-Engineered High-Entropy Metastable FCC $Cu_{2-y}Ag_y(In_xSn_{1-x})Se_2S$ Nanomaterials with High Thermoelectric Performance

Wanjia Zhang,[1,┼] Yue Lou,[1,┼] Hongliang Dong,[2] Fanshi Wu,[1] Janak Tiwari,[3] Zhan Shi,[4] Tianli Feng,[3] Sokrates T. Pantelides[5] and Biao Xu*[1]*

W. J. Zhang, Y. Lou, F. S. Wu, B. Xu
Department of Chemistry and Chemical Engineering, Nanjing University of Science and Technology, Nanjing, Jiangsu 210094, P.R. China
H. L. Dong
Center for High Pressure Science and Technology Advanced Research, Shanghai 201203, China
J. Tiwari, T. Feng
Department of Mechanical Engineering, The University of Utah, Salt Lake City, UT 84112, USA
Z. Shi
State Key Laboratory of Inorganic Synthesis and Preparative Chemistry, College of Chemistry, Jilin University, Changchun 130012, P.R. China
S. T. Pantelides
Department of Physics and Astronomy and Department of Electrical and Computer Engineering, Vanderbilt University, Nashville, TN 37235, USA

┼ These two authors contributed equally
*Corresponding Authors:
louyue@njust.edu.cn (Yue Lou)
xubiao@njust.edu.cn (Biao Xu)

Table of Contents

Experimental Procedures

Results and Discussion

Experimental Procedures

Chemicals. Oleylamine (OAm, 80~90%) and 1-dodecanethiol (DDT, 98%) were purchased from Shanghai Macklin Biochemical Technology Co., Ltd. Tin chloride dehydrate ($SnCl_2{\cdot}2H_2O$, 99.99%), indium chloride ($InCl_3$, 99.99%) and copper chloride (CuCl, 99.95%) were obtained from Aladdin Reagent Co. Ltd. Diphenyl diselenide (97%) was purchased from Energy Chemical. Silver nitrate ($AgNO_3$) and ethanol were obtained from Sinopharm Chemical Reagent Co., Ltd and Nanjing Chemical Reagent Co., Ltd. All chemicals were directly used without any purifying treatments.

Preparation of Cu_2SnSe_3 nanocrystals. Solution A: Diphenyl diselenide/OAm solution was prepared by dissolving diphenyl diselenide (2.3410 g, 7.5 mmol) in OAm (30 mL) at room temperature through sonicating for about 15 minutes. Solution B: CuCl (0.8910 g, 9 mmol), $SnCl_2{\cdot}2H_2O$ (0.6770 g, 3 mmol) and OAm (120 mL) were mixed in a 500 mL three-neck flask. The mixture was degassed at room temperature for several minutes followed by purging with N_2 under magnetic stirring. Subsequently, the mixture was heated to 230 °C, and solution A was rapidly injected into the mixture. Finally, the mixture was heated to 240 °C and held for 30min. After being cooled to room temperature naturally, the products were washed with ethanol and dried under a vacuum.

Preparation of Cu_2SnSe_2S nanocrystals. All the steps and parameters are the same as the preparation of Cu_2SnSe_3, except for the addition of DDT (15 mL) in Solution B.

Preparation of $Cu_2In_xSn_{1-x}Se_2S$ and $Cu_3InSnSe_3S_2$ nanocrystals. All the steps and parameters are the same as the preparation of Cu_2SnSe_2S, except for the addition of $InCl_3$ (3x mmol) in Solution B and the corresponding decrease in $SnCl_2{\cdot}2H_2O$ amount.

Preparation of $Cu_{2-y}Ag_y(In_{0.06}Sn_{0.94})Se_2S$ nanocrystals. All the steps and parameters are the same as the preparation of $Cu_2In_xSn_{1-x}Se_2S$, except for the addition of $AgNO_3$ and the corresponding decrease in CuCl amount.

Spark Plasma Sintering. The dense bulk matrixes compacted from nanocrystals were prepared by spark plasma sintering (SPS) system (LABOX-110, Sinter Land) at 673 K with an axial compressive stress of 50 MPa for 10 min under vacuum. The obtained pellets were then cut into a $3 \times 3 \times 10$ mm^3 rectangular bar and into a ∅10 × 1.5 mm disk.

Characterization. Synchrotron X-ray diffraction data were measured at BL17b in an energy state of 20 keV (0.62 Å). The pair distribution function G(r), correction, background subtraction, and sample absorption were completed by employing PDFgetX.[1] Structure refinements were accomplished by using PDFgui.[2] The crystalline phase of the samples was measured by powder X-ray diffraction (XRD; D8 ADVANCE, Bruker, Germany) with Cu Kα radiation ($\lambda = 1.5418$

Å) at a voltage of 40 kV and current of 40 mA. The microstructure of nanomaterials was investigated by transmission electron microscopy (TEM) and high-resolution transmission electron microscopy (HRTEM), taken by a Talos F200s transmission electron microscope operated at 200 kV. Elemental mapping images were acquired at the same instrument. Energy dispersive spectroscopy (EDS; JEOL JSM-6700F) was used for chemical composition analysis under an acceleration voltage of 10 kV. Atomic-resolution scanning transmission electron microscopy (STEM) images and energy-dispersive spectrometry (EDS) maps were acquired on an FEI-Titan Cubed Themis G2 300. STEM high angle annular dark field (STEM-HAADF) images were taken using an annular-type detector. The microstructure of the SPSed-samples pellets was characterized by a scanning electron microscope (SEM; FEI Scios 2 HiVac). X-ray photoelectron spectroscopy (XPS) was recorded by a PHI5000 Versa Probe system (ULVAC-PHI, Japan) with the monochromatic Al Kα line as the X-ray source. Atomic-scale composition analysis was conducted using atom probe tomography (APT). APT measurements were performed on a local electrode atom probe (LEAPTM 4000X Si, CAMECA) by applying 10-ps, 10-pJ ultraviolet (wavelength = 355 nm) laser pulses with a detection rate of 1 ion per 100 pulses on average, a pulse repetition rate of 200 kHz at a base temperature of 40 K, and an ion flight path of 160 mm. The corresponding 3D reconstructions and data analysis were processed using the IVASTM 3.8.0. Oxygen nitrogen hydrogen analyzer (ONH836) and carbon-sulfur analyzer (USA, LECO, CS844) were used for measurement of hydrogen and carbon concentrations in sintered nanomaterials.

Measurement of thermoelectric properties. The electrical conductivity and Seebeck coefficient were measured simultaneously by the static direct current method and four-probe method (CTA-3S, CRYALL). The measuring uncertainty of σ and S was ~ 5%. The thermal conductivity was calculated by $\kappa = C_p \cdot \rho \cdot D$, in which the specific heat at constant pressure (C_p) was obtained by using a differential scanning calorimetry thermalanalyzer (DSC 404 F3, NETZSCH), the pellet density (ρ) was calculated by Archimedes method and the thermal diffusivity (D) was measured using the laser flash method (Discovery Xeon Flash, TA Instrument). The measurement uncertainty of thermal conductivity κ was estimated to be within 10%, and thus the combined uncertainty for all measurements involved in ZT determination is below 20%. Charge carrier concentration (n_H) and Hall mobility (μ_H) were determined from the Hall coefficient (R_H) measurement using the Van der Pauw method under a reversible magnetic field of 1.5 T (Lake Shore 8400 Series, Model 8404, USA), and from $n_H = 1/eR_\mathrm{H}$ and $\mu_H = \sigma R_H$, respectively. Low-temperature constant-pressure heat capacities (C_p) were measured using a Quantum Design Physical Properties Measurement System (QD-PPMS) with logarithmic T spacings over 2 – 250 K repeating three times at each temperature point. Thermogravimetric analysis (TGA) was carried out on a thermal gravimetric analyzer (TGA 5500).

DFT calculation.

Electronic band structures: All calculations were performed within the first-principles density functional theory (DFT) formalism as implemented in the Vienna Ab-initio Simulation Package (VASP).[3] The structural optimizations and self-consistent calculations were carried out using the Perdew-Burke-Ernzerhof (PBE) generalized gradient approximation exchange functional plus the effective Hubbard *U* of the Dudarev et al's approach.[4] In this work, the on-site effective U = 10 eV was introduced to describe the localization characteristic of copper's 3d block. The cutoff energy was set to 500 eV and the energy conversion criterion of 1×10^{-6} eV per atom was used for the calculation of the electronic band structure. In the structural optimization, we constrained the cell parameters onto the experimental data and optimized the atomic coordinates until the Hellman-Feynman forces fell below 10^{-3} eV/Å.

Phonon band structures: The phonon band structure, group velocity, specific heat, density of states are calculated by using Phonopy[5] and VASP. The plane-wave energy cutoff is 500 eV. The energy convergence threshold is 10^{-8} eV per atom. The cubic Cu_2SnSe_3, under virtual crystal approximation, has 2 atoms per primitive cell. The monoclinic Cu_2SnSe_3 has 12 atoms per primitive cell. In the primitive cell relaxations, we use 10^{-6} and 10^{-4} eV/Å for the force convergence threshold for the cubic and monoclinic Cu_2SnSe_3, respectively. The **k**-mesh during the primitive cell relaxations are 16×16×16 and 9×9×9 for the cubic and monoclinic Cu_2SnSe_3, respectively. 4×4×4 and 3×3×3 supercells are used for the calculation of phonon dispersion for cubic and monoclinic Cu_2SnSe_3, respectively. The **k**-mesh used in the supercell calculations is 3×3×3.

Formation Energy Calculation. In general, the formation energy for a compound is calculated by using the equation given below:[6]

$$\Delta H_f = E_{tot} - \sum_i \mu_i \, x_i \qquad (S1)$$

where E_{tot} is the DFT total energy of the compound, μ_i is the chemical potential of element i, and x_i is the quantity of element i in the compound.

The calculation details of Lorentz factor (L) and density of states effective mass (m_d^*) via single parabolic band (SPB) model. In the case of electron scattering by the acoustical vibrations of the lattice atoms, the Lorenz number can be expressed as:[7]

$$L = \left(\frac{k_B}{e}\right)^2 \frac{3F_0(\eta)F_2(\eta) - 4F_1^2(\eta)}{F_0^2(\eta)} \qquad (S2)$$

Assuming the acoustic scattering for all investigated samples is prominent ($\lambda=0$), the m_d^* can be acquired from the experimental data S and p by using the following equations:

$$S = \frac{k_B}{e}\left[\frac{(\lambda+2)F_{(\lambda+1)}(\eta)}{(\lambda+1)F_{\lambda}(\eta)} - \eta\right] \qquad (S3)$$

$$m_d^* = \frac{h^2}{2k_BT}\left(\frac{p}{4\pi F_{1/2}(\eta)}\right)^{2/3} \qquad (S4)$$

$$F_j(\eta) = \int_0^{\infty} \frac{x^j}{1 - e^{x-\eta}} dx \qquad (S5)$$

where $F_j(\eta)$ is the Fermi integral of order j, η is the reduced Fermi level $E_f/\kappa_B T$ and h is the Planck constant.

The calculation details of heat capacity C_P via the Debye-3 Einstein model. The plot of C_p vs T could be well fitted to a sum of Debye and Einstein models ranging from 100-200 K as the following equation[8-10]:

$$C_{ph}(T) = 9R\frac{\sum_{i=1}^{3} a_i}{n-1} x_D^{-3} \int_0^{x_D} \frac{x^4 e^x}{(e^x - 1)^2} dx + 3R\sum_{i=1}^{3}[a_i \frac{x_{E_i}^2 e^{xE_i}}{(e^{xE_i} - 1)^2}] \qquad (S6)$$

where $x_D = \theta_D/T$, $x_E = \theta_E/T$, and θ_D, θ_E are the Debye and Einstein temperatures, respectively. The constant R is the molar gas constant. The parameter n is the number of atoms per molecular formula. The letters are adjustable, and the subscript i represents the degeneracy of the multiple optical branches. The various fitting parameters are listed in Table S4.

Results and Discussion

1. Crystal structure characterization

As shown in Fig. S1, for Cu_2SnSe_3, Cu_2SnSe_2S, $Cu_2In_xSn_{1-x}Se_2S$ (x=0.06, 0.14, 0.25), the peak at 26.8° can be indexed to the (111) plane of the cubic structure of $Cu_{1.8}Se$ phase, which indicates the existence of a small quantity of the second phase. And we can observe that $Cu_{1.8}Se$ phase disappeared when the amount of In increased, and finally $Cu_2In_{0.4}Sn_{0.6}Se_2S$ and $Cu_3InSnSe_3S_2$ nanocrystals without the second phase were obtained. This phenomenon demonstrates that the main reason of the formation of $Cu_{1.8}Se$ second phase is feed ratio of metal salts. When the amount of In is small, excess Se will reacted with Cu to obtain $Cu_{1.8}Se$.

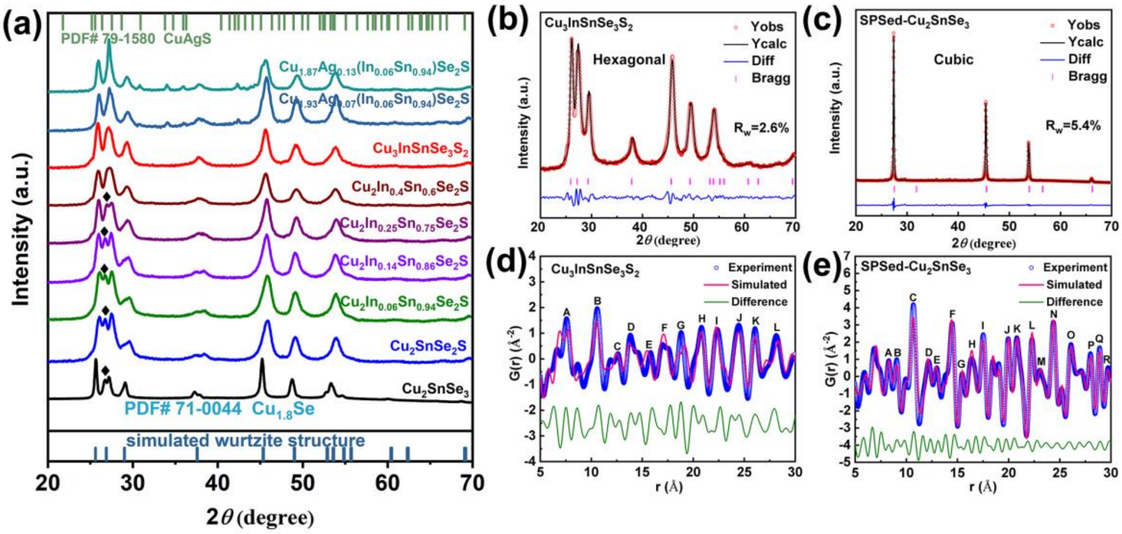

Fig. S1 (a) Powder X-ray diffraction (PXRD) patterns of solution-synthesized samples. Rietveld refinement results of (b) solution-synthesized $Cu_3InSnSe_3S_2$ and (c) SPSed-Cu_2SnSe_3. PDF fit to G(r) function at the range of 5-30 Å by using the hexagonal model for (d) solution-synthesized $Cu_3InSnSe_3S_2$ and cubic model for (e) SPSed-Cu_2SnSe_3.

Table S1. The cell parameters of solution-synthesized and SPSed-samples from Rietveld refinement data.

Parameter	Solution-synthesized $Cu_3InSnSe_3S_2$	SPSed-Cu_2SnSe_3	SPSed-$Cu_3InSnSe_3S_2$	SPSed-$Cu_{1.93}Ag_{0.07}(In_{0.06}Sn_{0.94})Se_2S$
space group	$P6_3mc$	Fm-3m	I-42m	Fm-3m
a	3.982 Å	5.6636 Å	5.6378 Å	5.6421 Å
b	3.982 Å	5.6636 Å	5.6378 Å	5.6421 Å
c	6.578 Å	5.6636 Å	11.2620 Å	5.6421 Å
α	90°	90°	90°	90°
β	90°	90°	90°	90°
γ	120°	90°	90°	90°

As demonstrated in Fig. S2, metastable wurtzite Cu_2SnSe_3 nanocrystals with uniform size and morphology is firstly synthesized via colloid synthesis. Then S is incorporated into the anionic site and Ag, In are alloyed at the cationic site through well controlling the balance of precursors reactivity in colloidal synthesis. Subsequently, based on size reduction and entropy optimization engineering of our solution-synthesized nanocrystals, a series of high-entropy multinary chalcogenides nanostructured solid with metastable cubic phase are obtained, which is different from the conventional monoclinic phase synthesized via solid-state synthesis, as exemplified by melting. Besides, when the amount of indium increases to a certain amount, SPSed-$Cu_2In_{0.4}Sn_{0.6}Se_2S$ and SPSed-$Cu_3InSnSe_3S_2$ nanostructured solid have a tetragonal structure (space group *I*-42*m*), and this tetragonal unit cell can be approximately depicted as a 1x1x2 supercell of cubic Cu_2SnSe_3.

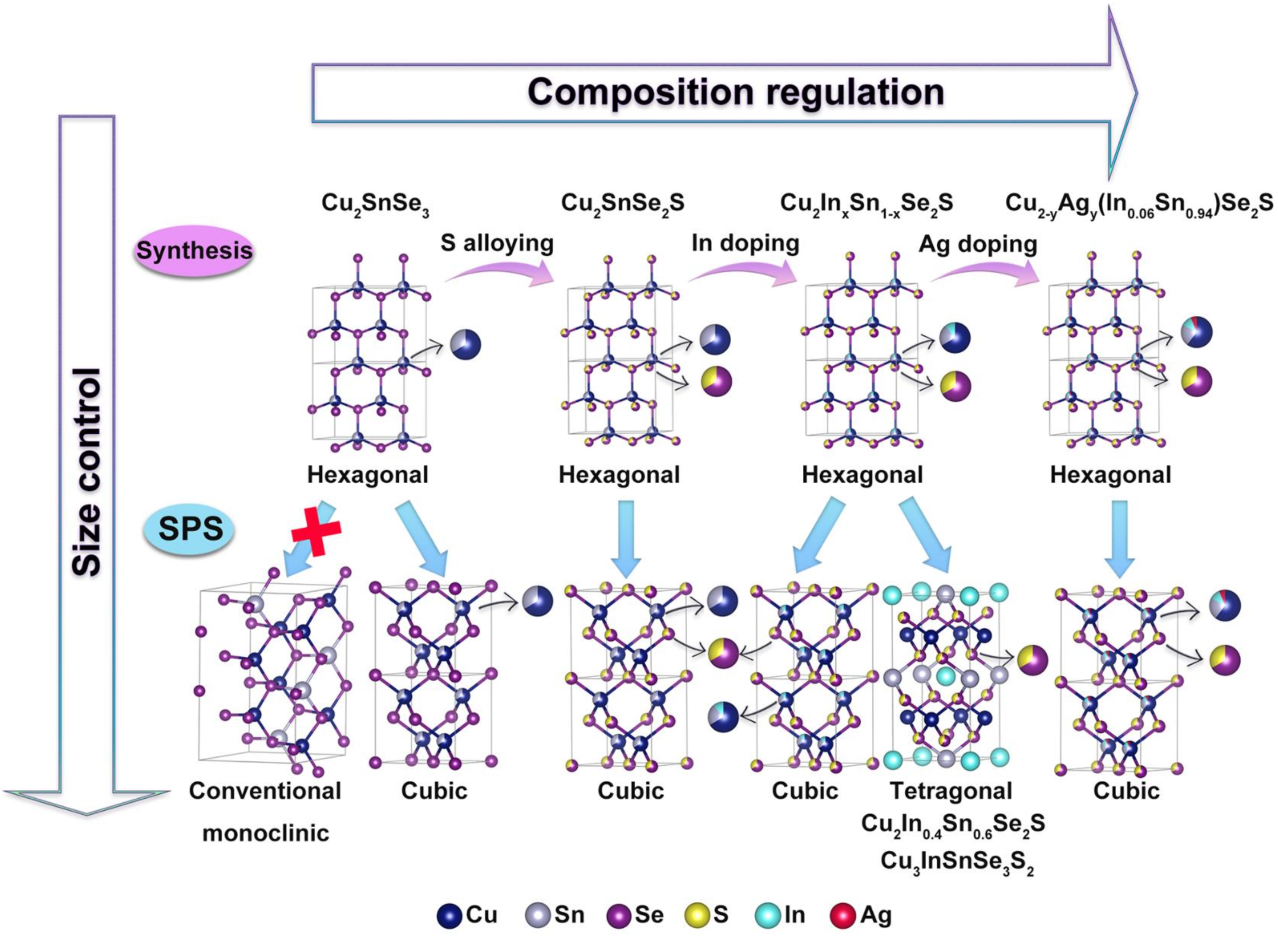

Fig. S2 Crystal structures for synthesized and SPSed-Cu_2SnSe_3, Cu_2SnSe_2S, $Cu_2In_xSn_{1-x}Se_2S$ (x=0.02-0.25), $Cu_2In_{0.4}Sn_{0.6}Se_2S$, $Cu_3InSnSe_3S_2$ and $Cu_{2-y}Ag_y(In_{0.06}Sn_{0.94})Se_2S$ (y=0.07, 0.13).

Table S2. Calculated formation energy (ΔH_f) for different phase structures via DFT using the Vienna ab initio simulation package (VASP).

Phase / Sample	Monoclinic (eV·atom^{-1})	Cubic (eV·atom^{-1})	Tetragonal (eV·atom^{-1})
SPSed-Cu_2SnSe_3	-2.4564	-2.4529	/
SPSed-Cu_2SnSe_2S	-2.5603	-2.5519	/
SPSed-$Cu_2In_{0.06}Sn_{0.94}Se_2S$	-2.5523	-2.5435	/
SPSed-$Cu_3InSnSe_3S_2$	-3.3915	-3.3863	-3.3994
SPSed-$Cu_{1.87}Ag_{0.13}(In_{0.06}Sn_{0.94})Se_2S$	-2.5816	-2.5730	/

Table S3. Table peaks assignment to the atomic pair in SPSed-Cu_2SnSe_3, solution-synthesized $Cu_3InSnSe_3S_2$, SPSed-$Cu_3InSnSe_3S_2$ and SPSed-$Cu_{1.93}Ag_{0.07}(In_{0.06}Sn_{0.94})Se_2S$, respectively.

SPSed-Cu_2SnSe_3:

label	atomic pair	atomic pair distances(Å)
A	Se-Cu/(Sn)	8.26
B	Se-Se; Cu-Cu/(Sn); Sn-Sn	9.02
C	Se-Se	10.65
D	Se-Se; Cu-Cu/(Sn); Sn-Sn	12.16
E	Se-Cu/(Sn)	12.94
F	Se-Se; Cu-Cu/(Sn); Sn-Sn	14.43
G	Se-Se	15.42
H	Cu-Cu/(Sn); Sn-Sn	16.36
I	Se-Se; Cu-Cu/(Sn); Sn-Sn	17.50
J	Se-Se; Cu-Cu/(Sn); Sn-Sn	19.95
K	Cu-Cu/(Sn); Sn-Sn	20.80
L	Se-Se; Cu-Cu/(Sn); Sn-Sn	22.27
M	Se-Se; Se-Cu/(Sn)	23.05
N	Se-Se; Cu-Cu/(Sn); Sn-Sn	24.38
O	Se-Cu/(Sn)	26.10
P	Se-Se	28.00
Q	Se-Cu/(Sn)	28.87
R	Se-Cu/(Sn)	29.79

Solution-synthesized $Cu_3InSnSe_3S_2$:

label	atomic pair	atomic pair distances(Å)
A	Se-Se; S-S; Se-S	7.56
B	Se-Se; S-S; Se-S; Cu-Cu/(In)/(Sn); In-In/(Sn); Sn-Sn	10.57
C	Se-Cu/(In)/(Sn); S-Cu/(In)/(Sn);	12.62
D	Cu-Cu/(In)/(Sn); In-In/(Sn); Sn-Sn; Se-Cu/(In)/(Sn); S-Cu/(In)/(Sn)	13.83
E	Se-Cu/(In)/(Sn); S-Cu/(In)/(Sn)	15.80
F	Se-Se; S-S; Se-S; Se-Cu/(In)/(Sn); S-Cu/(In)/(Sn)	16.99
G	Cu-Cu/(In)/(Sn); In-In/(Sn); Sn-Sn	18.79
H	Se-Se; S-S; Se-S; Cu-Cu/(In)/(Sn); In-In/(Sn); Sn-Sn	20.79
I	Se-Se; S-S; Se-S; Cu-Cu/(In)/(Sn); In-In/(Sn); Sn-Sn	22.34
J	Cu-Cu/(In)/(Sn); In-In/(Sn); Sn-Sn; Se-Cu/(In)/(Sn); S-Cu/(In)/(Sn)	24.45
K	Se-Cu/(In)/(Sn); S-Cu/(In)/(Sn)	26.05
L	Se-Se; S-S; Se-S	28.15

SPSed-$Cu_3InSnSe_3S_2$:

label	atomic pair	atomic pair distances(Å)
A	S-In; Se-In	8.23
B	Se-Se; S-S; Se-S	9.01
C	S-In; Se-In; Cu-Cu; In-In	10.64
D	S-In; Se-In	12.17
E	S-In; Se-In	12.91
F	Se-Se; S-S; Se-S	14.40
G	S-Cu; Se-Cu	16.27
H	Se-Se; S-S; Se-S; In-In	17.44
I	Cu-In	19.88
J	In-In	20.74
K	Se-Se; S-S; Se-S; S-Cu; Se-Cu	22.20
L	Se-Se; S-S; Se-S	22.97
M	Se-Se; S-S; Se-S; S-In; Se-In	24.27
N	Cu-In	26.01
O	Cu-In	27.88
P	S-Cu; Se-Cu	28.79
Q	S-Cu; Se-Cu	29.61

SPSed-$Cu_{1.93}Ag_{0.07}(In_{0.06}Sn_{0.94})Se_2S$:

label	atomic pair	atomic pair distances(Å)
A	Se-Se; S-S; Se-S	6.89
B	Se-Cu/(In)/(Sn)/(Ag); S-Cu/(In)/(Sn)/(Ag)	8.33
C	Se-Se; S-S; Se-S; Cu-Cu/(In)/(Sn)/(Ag); In-In/(Sn)/(Ag); Sn-Sn/(Ag); Ag-Ag	9.07
D	Se-Se; S-S; Se-S	10.64
E	Se-Se; S-S; Se-S; Cu-Cu/(In)/(Sn)/(Ag); In-In/(Sn)/(Ag); Sn-Sn/(Ag); Ag-Ag	12.07
F	Se-Cu/(In)/(Sn)/(Ag); S-Cu/(In)/(Sn)/(Ag)	12.86
G	Se-Se; S-S; Se-S; Cu-Cu/(In)/(Sn)/(Ag); In-In/(Sn)/(Ag); Sn-Sn/(Ag); Ag-Ag	14.38
H	Cu-Cu/(In)/(Sn)/(Ag); In-In/(Sn)/(Ag); Sn-Sn/(Ag); Ag-Ag	16.45
I	Se-Se; S-S; Se-S; Cu-Cu/(In)/(Sn)/(Ag); In-In/(Sn)/(Ag); Sn-Sn/(Ag); Ag-Ag	17.43
J	Se-Se; S-S; Se-S; Cu-Cu/(In)/(Sn)/(Ag); In-In/(Sn)/(Ag); Sn-Sn/(Ag); Ag-Ag	19.93
K	Cu-Cu/(In)/(Sn)/(Ag); In-In/(Sn)/(Ag); Sn-Sn/(Ag); Ag-Ag	20.79
L	Se-Se; S-S; Se-S; Cu-Cu/(In)/(Sn)/(Ag); In-In/(Sn)/(Ag); Sn-Sn/(Ag); Ag-Ag	22.22
M	Se-Se; S-S; Se-S; Se-Cu/(In)/(Sn)/(Ag); S-Cu/(In)/(Sn)/(Ag)	23.02
N	Se-Se; S-S; Se-S; Cu-Cu/(In)/(Sn)/(Ag); In-In/(Sn)/(Ag); Sn-Sn/(Ag); Ag-Ag	24.32
O	Se-Cu/(In)/(Sn)/(Ag); S-Cu/(In)/(Sn)/(Ag)	26.02
P	Se-Se; S-S; Se-S	27.95
Q	Se-Cu/(In)/(Sn)/(Ag); S-Cu/(In)/(Sn)/(Ag)	28.84

2. Microstructure and composition

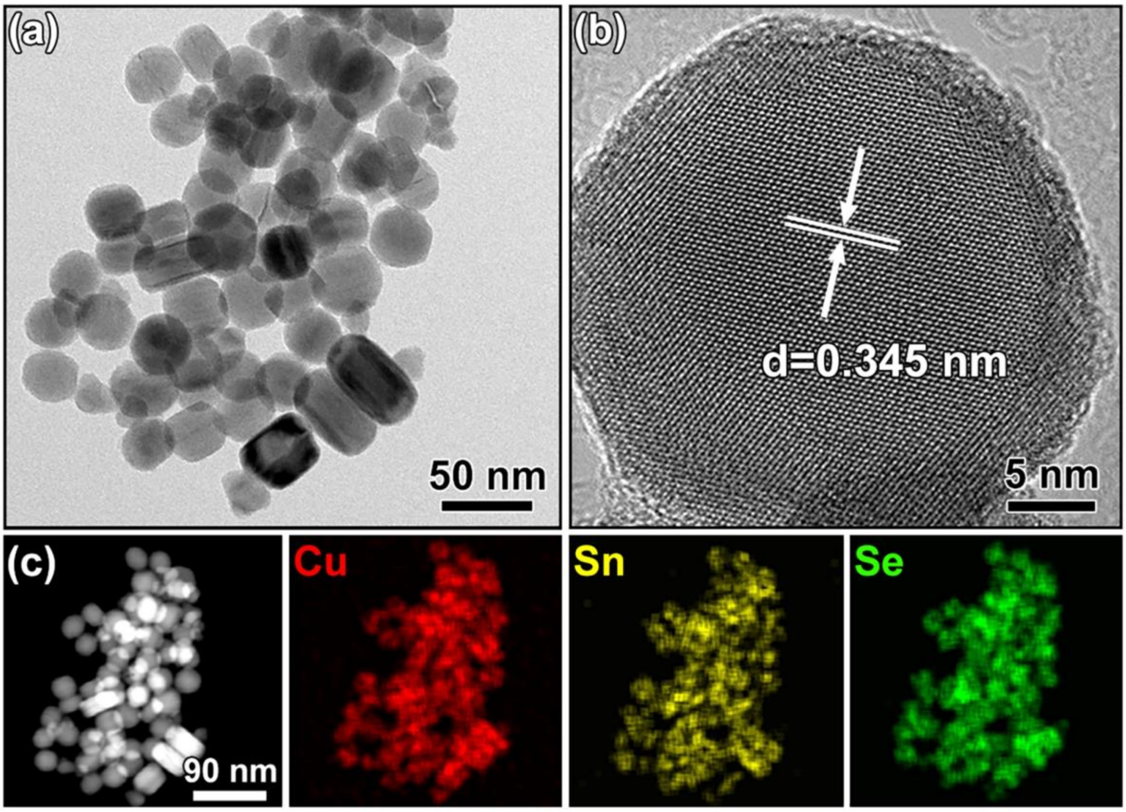

Fig. S3 (a) Low-magnification TEM image, (b) HRTEM image, (c) EDS elemental mapping images of solution-synthesized Cu_2SnSe_3.

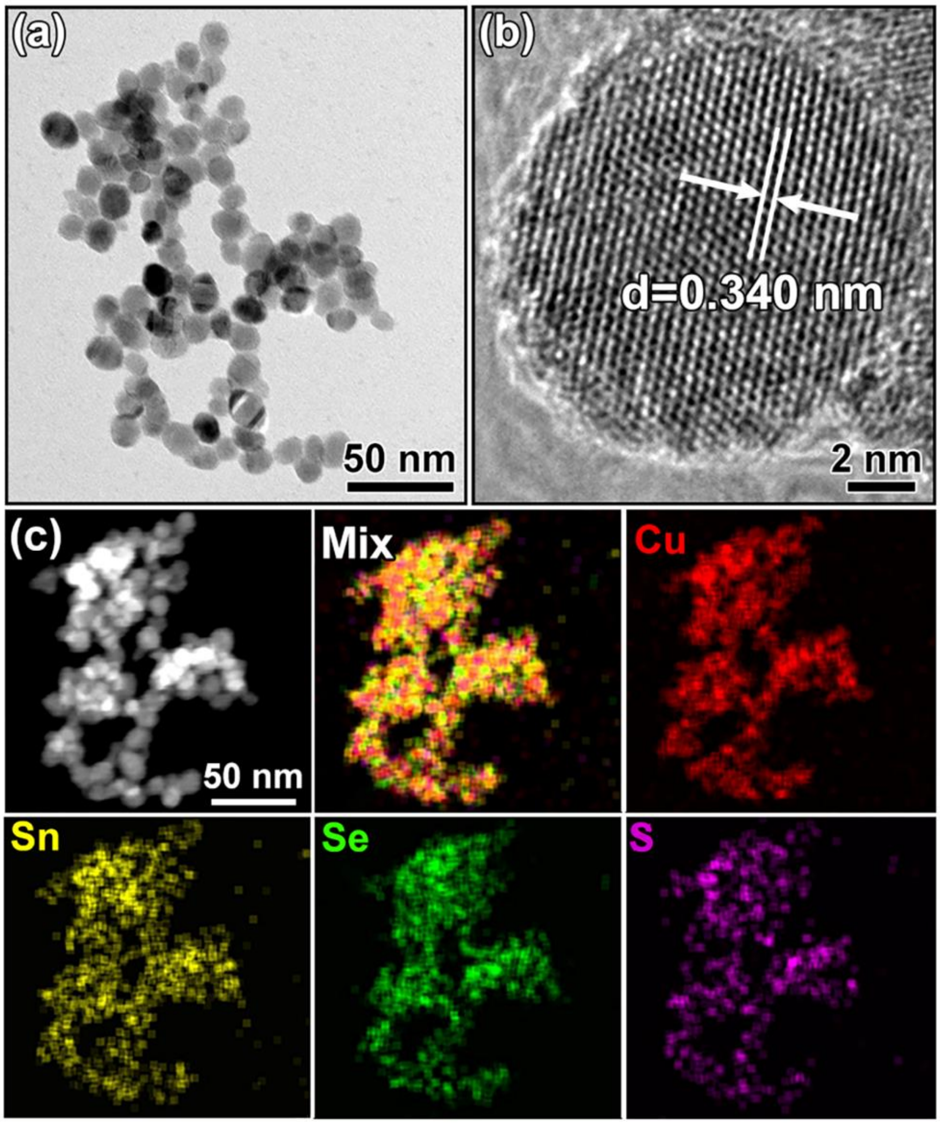

Fig. S4 (a) Low-magnification TEM image, (b) HRTEM image, (c) EDS elemental mapping images of solution-synthesized Cu_2SnSe_2S.

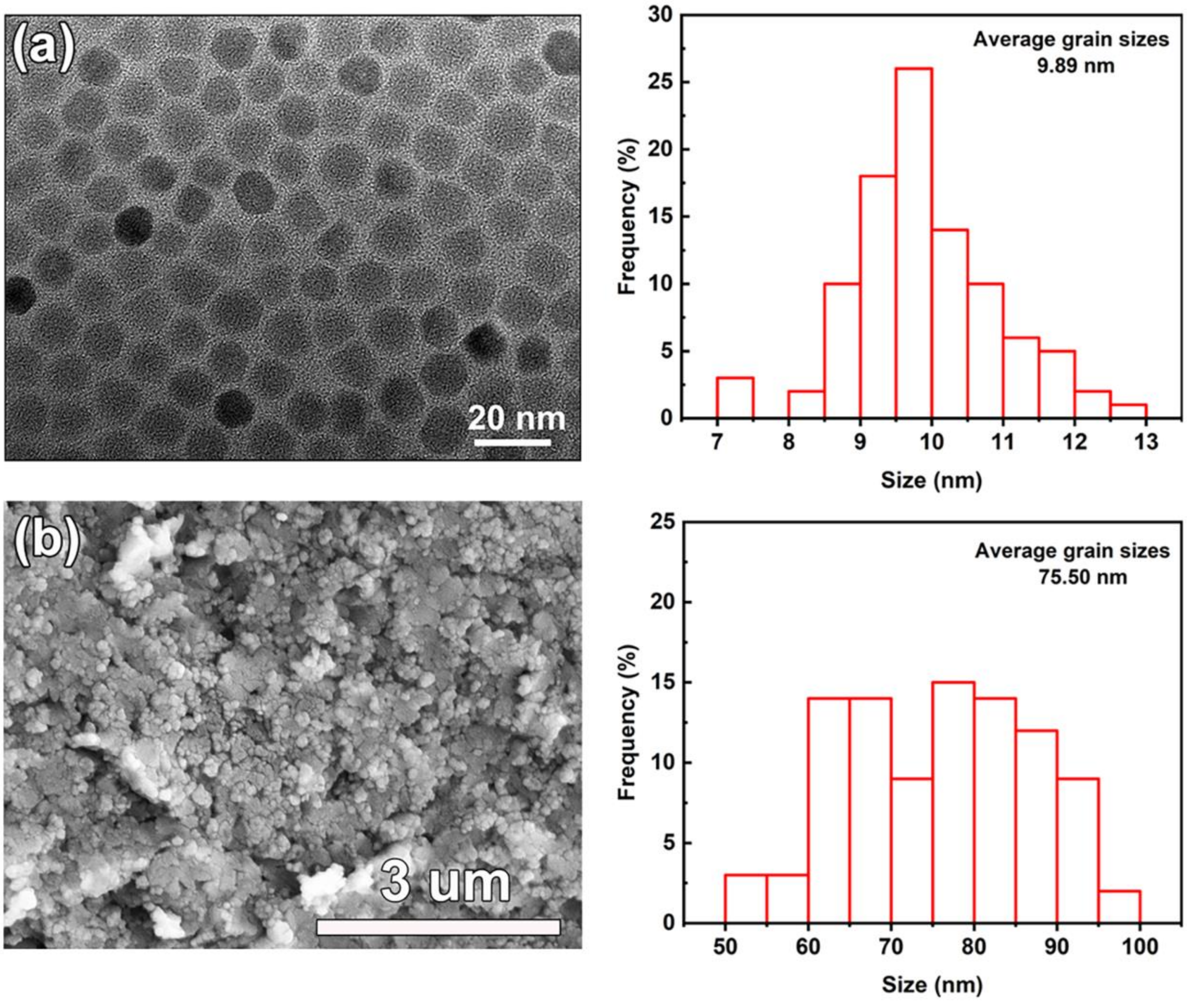

Fig. S5 (a) Low-magnification TEM image of solution-synthesized $Cu_3InSnSe_3S_2$ and (b) SEM micrograph of SPSed-$Cu_3InSnSe_3S_2$ sample.

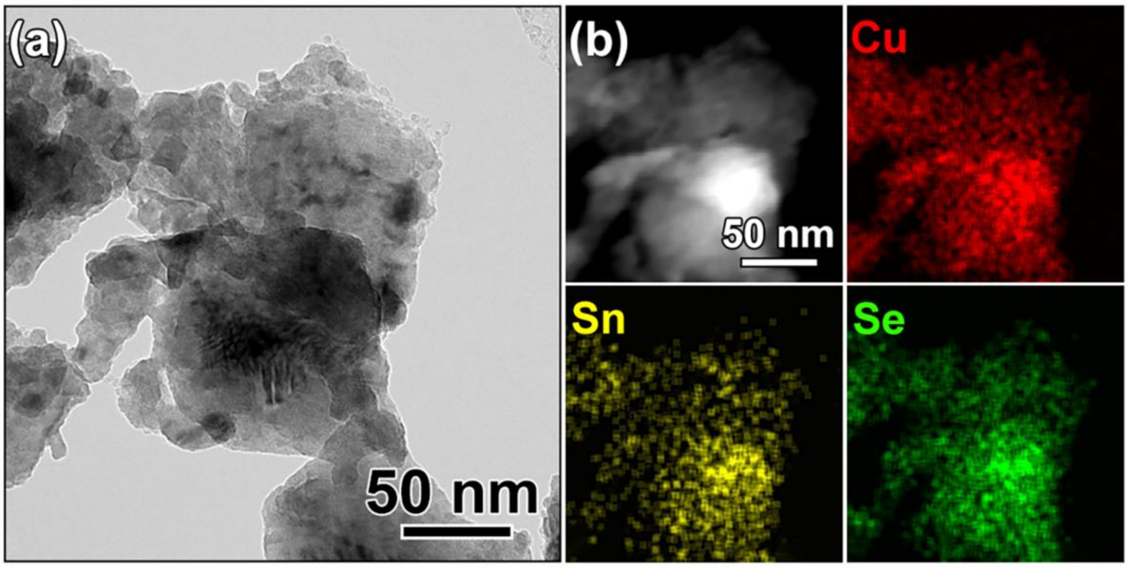

Fig. S6 (a) Low-magnification TEM image and (b) EDS elemental mapping images of SPSed-Cu_2SnSe_3.

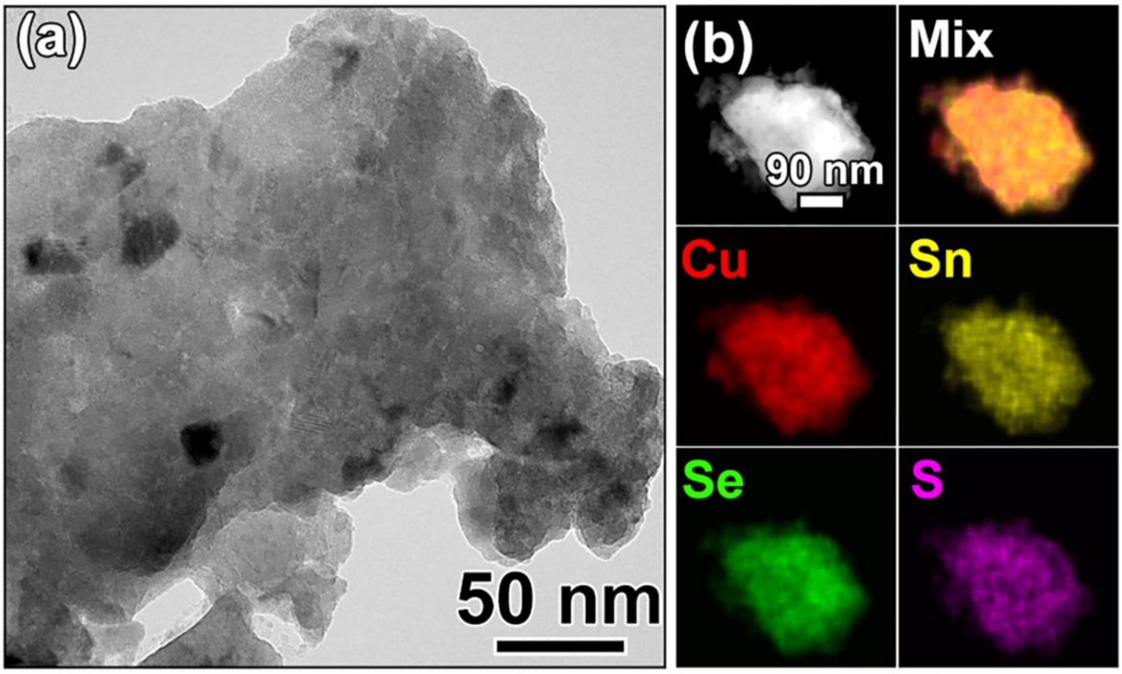

Fig. S7 (a) Low-magnification TEM image and (b) EDS elemental mapping images of SPSed-Cu_2SnSe_2S.

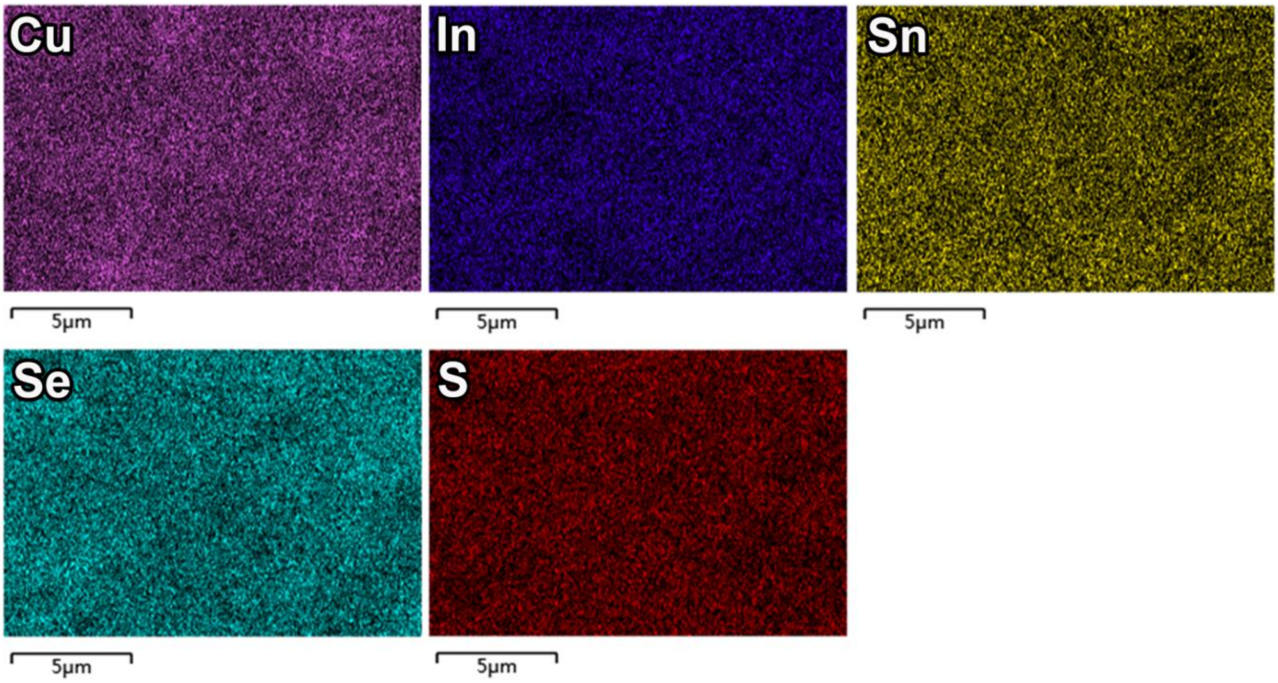

Fig. S8 The SEM/EDS mapping of SPSed-$Cu_3InSnSe_3S_2$.

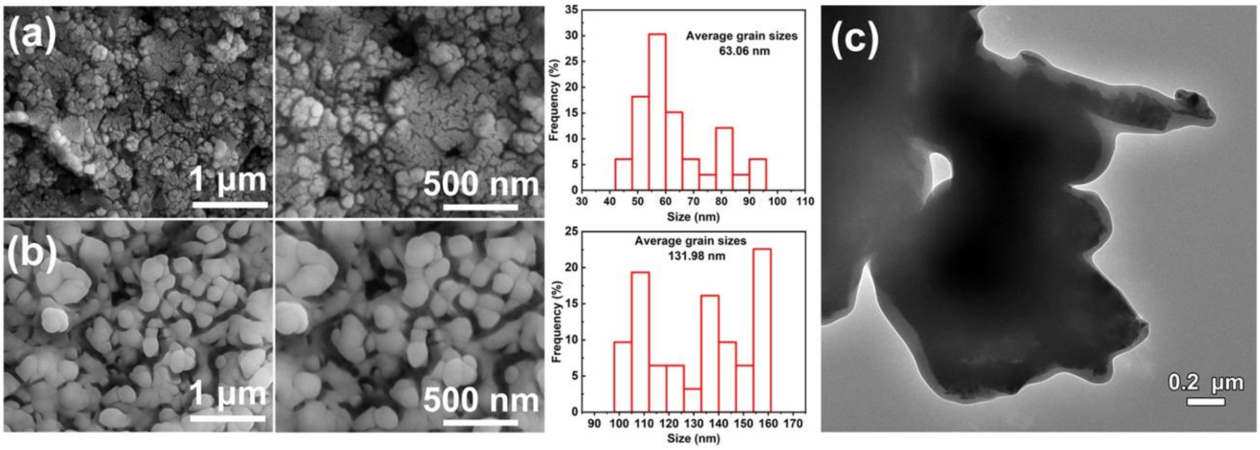

Fig. S9 SEM micrographs of (a) SPSed-$Cu_2In_{0.06}Sn_{0.94}Se_2S$ and (b) SPSed-$Cu_{1.87}Ag_{0.13}(In_{0.06}Sn_{0.94})Se_2S$ pellets. (c) The TEM image of SPSed-$Cu_{1.87}Ag_{0.13}(In_{0.06}Sn_{0.94})Se_2S$, exhibiting the organic hydrocarbons between nanocrystals of nanosructured solids during sintering process.

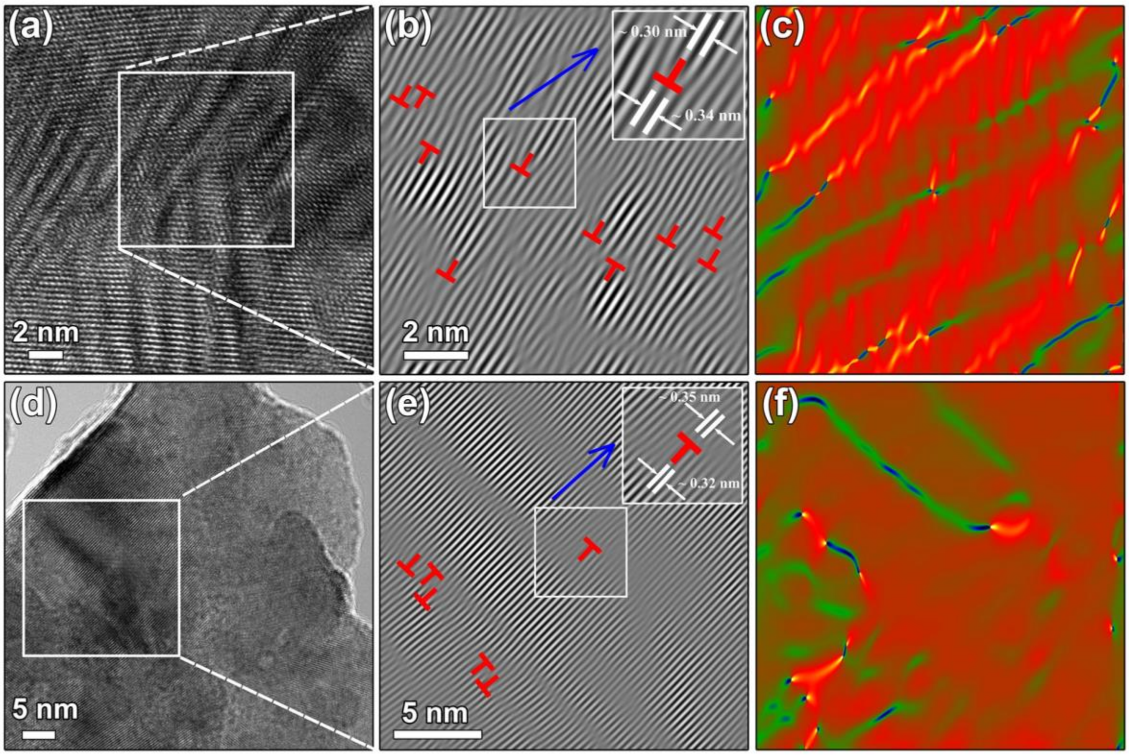

Fig. S10 HRTEM images of the dislocations in (a) SPSed-Cu_2SnSe_3 and (d) SPSed-Cu_2SnSe_2S samples. (b and e) The corresponding inverse FFT (IFFT) images of boxed region in (a) and (d), inset is the enlarged view of boxed region. (c and f) The corresponding strain mappings of (b) and (e), showing the dislocations cores with the high intensity.

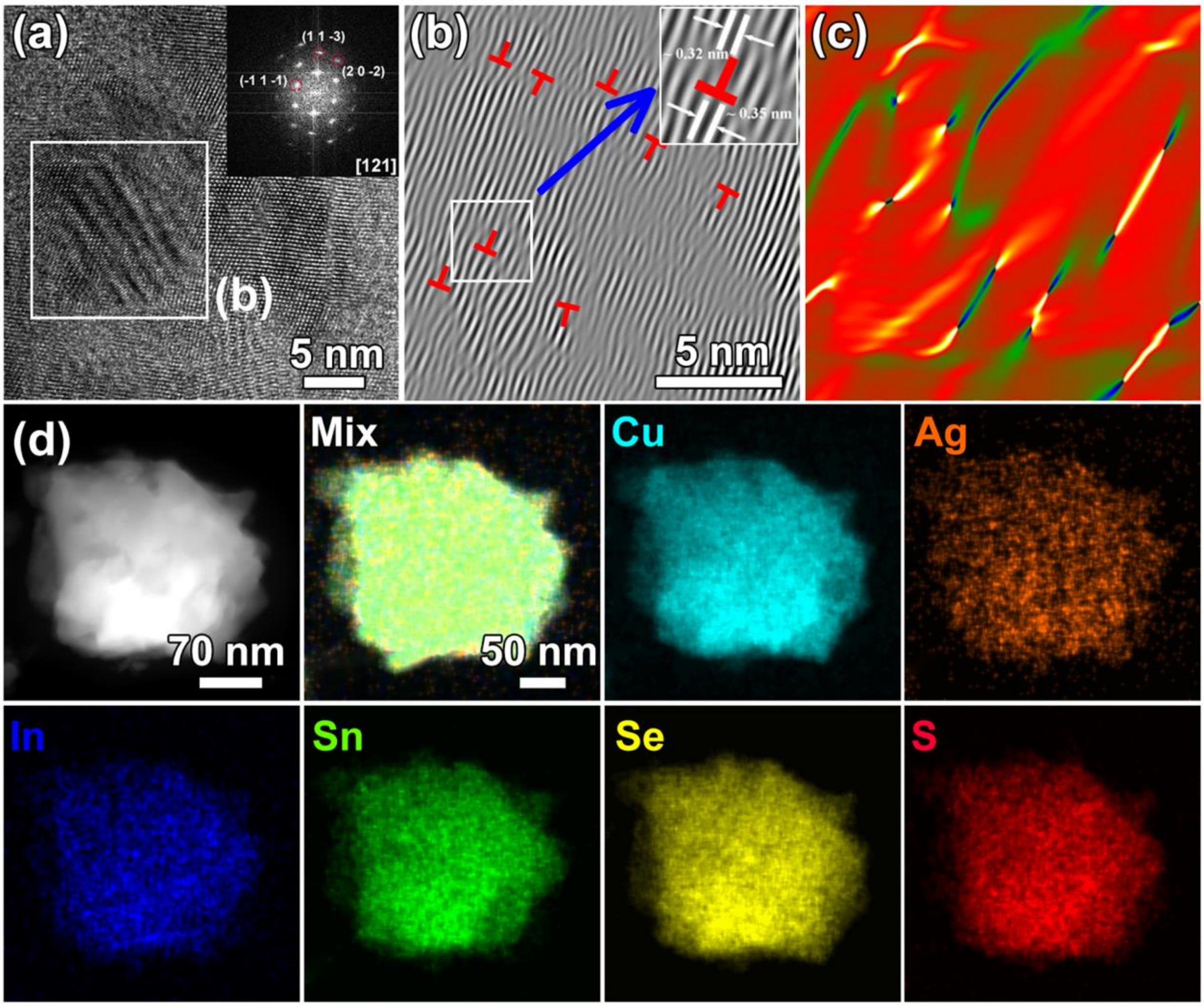

Fig. S11 HRTEM image of the dislocations in (a) SPSed-$Cu_{1.87}Ag_{0.13}(In_{0.06}Sn_{0.94})Se_2S$ sample, inset is the corresponding FFT along the [121] zone axis. (b) The corresponding inverse FFT (IFFT) image of boxed region in (a), inset is the enlarged view of boxed region. (c) The corresponding strain mapping of (b), showing the dislocations cores with high intensity. (d) EDS elemental mapping images of SPSed-$Cu_{1.87}Ag_{0.13}(In_{0.06}Sn_{0.94})Se_2S$ sample.

EDS analysis was used to quantify the elemental composition of solution-synthesized and SPSed-samples, as shown in Fig. S10. The EDS result of Cu_2SnSe_3 is shown in Fig. S10a, indicating that the atomic ratio of Cu: Sn: Se is 2.24: 1: 3.24. Then DDT was added as a sulfur source to prepare Cu_2SnSe_2S. The EDS spectra of $Cu_2In_{0.06}Sn_{0.94}Se_2S$ and SPSed-$Cu_2In_{0.06}Sn_{0.94}Se_2S$ are shown in Figs. S10c and f, proving the successful incorporation of In. And the composition of as-synthesized nanocrystals remains unchanged after the sintering process. Additionally, the In content in the nanocrystals increases almost linearly with increasing In content in the precursors. When a 1:1 ratio of $SnCl_2{\cdot}2H_2O$ to $InCl_3$ was used for the synthesis, the atom ratio of Cu: In: Sn: Se: S is around 3:1:1:3:2, which further verifies that the resulting products are $Cu_3InSnSe_3S_2$.

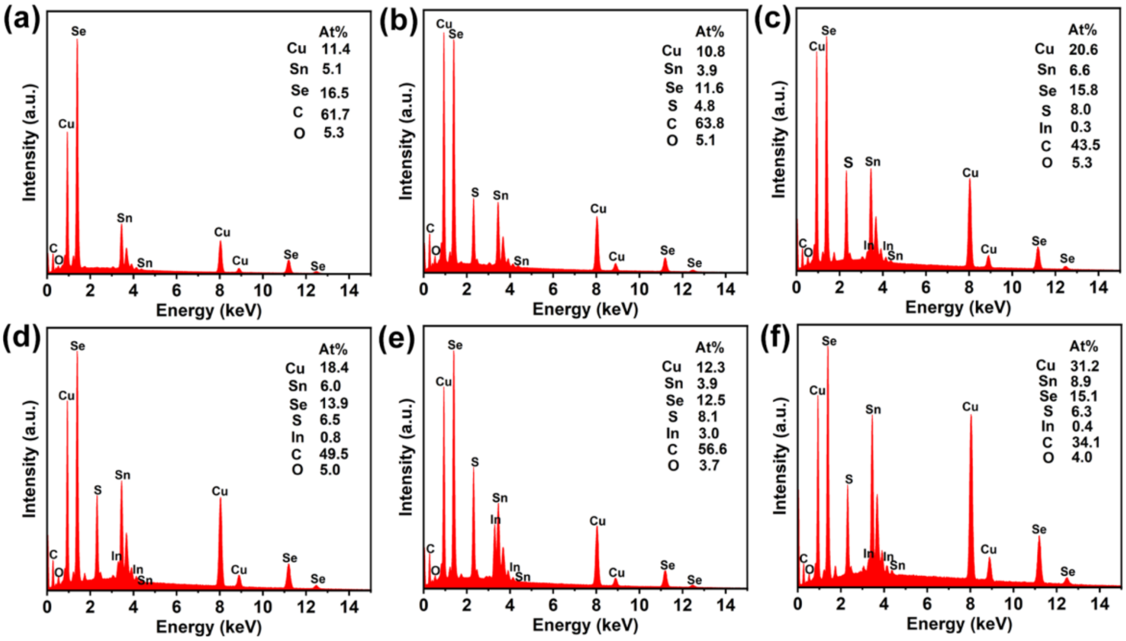

Fig. S12 EDS results of (a) solution-synthesized Cu_2SnSe_3, (b) solution-synthesized Cu_2SnSe_2S, (c) solution-synthesized $Cu_2In_{0.06}Sn_{0.94}Se_2S$, (d) solution-synthesized $Cu_2In_{0.14}Sn_{0.86}Se_2S$, (e) solution-synthesized $Cu_3InSnSe_3S_2$ and (f) SPSed-$Cu_2In_{0.06}Sn_{0.94}Se_2S$.

X-ray photoelectron spectroscopy (XPS) was performed to disclose the valence states of each element on the surface in the solution-synthesized $Cu_2In_{0.06}Sn_{0.94}Se_2S$ and SPSed-$Cu_2In_{0.06}Sn_{0.94}Se_2S$, as shown in Fig. S11. No peaks of other elements than Cu, In, Sn, Se, S, C, and O are observed in XPS survey spectrum, which agrees well with the EDS results. The dual peaks of Cu 2p for $Cu_2In_{0.06}Sn_{0.94}Se_2S$ at 932.0 eV and 951.8 eV with a separation of 19.8 eV reveal the presence of Cu with a valence of +1, and no satellite peak caused by Cu with +2 valence is found.[11-13] It is worth mentioning that the valence state of Cu changed before and after sintering. The binding energy of SPSed-$Cu_2In_{0.06}Sn_{0.94}Se_2S$ at the Cu 2p region could be divided into four peaks. The peaks located at 932.3 eV and 952.3 eV are associated with Cu^+ $2p_{3/2}$ and $2p_{1/2}$, respectively, and the peaks located at 934.5 eV and 954.7 eV are assigned to Cu^{2+} $2p_{3/2}$ and $2p_{1/2}$, respectively.[14] The In 3d peaks of $Cu_2In_{0.06}Sn_{0.94}Se_2S$ and SPSed-$Cu_2In_{0.06}Sn_{0.94}Se_2S$ at 444.6 eV and 452 eV can be assigned to In with a valence of +3.[11-13] The peaks of Sn 3d for $Cu_2In_{0.06}Sn_{0.94}Se_2S$ and SPSed-$Cu_2In_{0.06}Sn_{0.94}Se_2S$ at 486.3 eV and 494.7 eV are characteristic for Sn with a valence of +4.[11-13] The Se 3d peak at 54 eV for $Cu_2In_{0.06}Sn_{0.94}Se_2S$ and SPSed-$Cu_2In_{0.06}Sn_{0.94}Se_2S$ correspond to Se with a valence of -2.[15,16] In addition, we can find that another peak located at 58.8 eV for $Cu_2In_{0.06}Sn_{0.94}Se_2S$ was attributed to Se substance,[14] demonstrating excessive Se in raw materials. However, the Se substance peak disappears after sintering, indicating that part of Se volatilizes or reacts with Cu to form $Cu_{1.8}Se$ during the sintering process, which explains the existence of Cu^{2+} in the SPSed-sample. The corresponding peaks for the S $2p_{3/2}$ and $2p_{1/2}$ orbitals of bivalent sulfide ions (S^{2-}) are observed at 160.5 and 165.4 eV of $Cu_2In_{0.06}Sn_{0.94}Se_2S$ and SPSed-$Cu_2In_{0.06}Sn_{0.94}Se_2S$, respectively.[12]

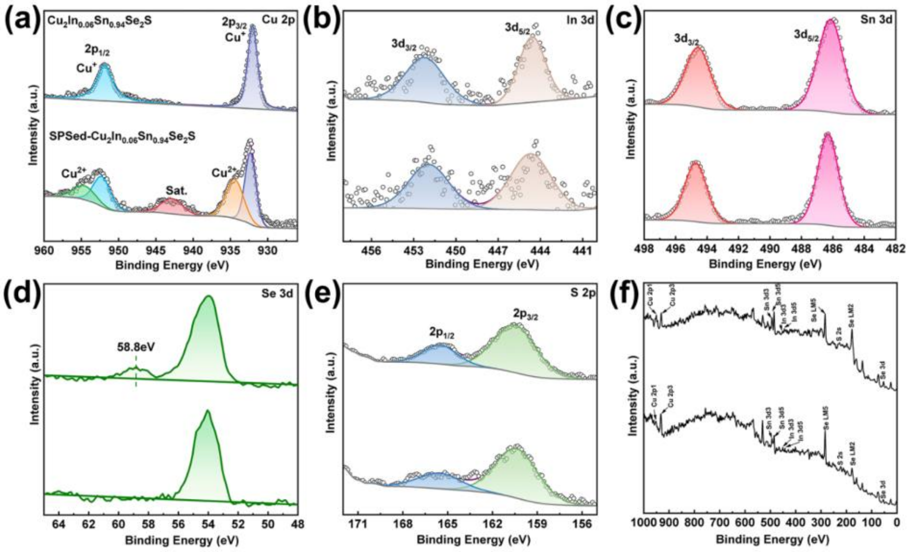

Fig. S13 XPS spectra of the solution-synthesized $Cu_2In_{0.06}Sn_{0.94}Se_2S$ and SPSed-$Cu_2In_{0.06}Sn_{0.94}Se_2S$ (a) Cu 2p, (b) In 3d, (c) Sn 3d, (d) Se 3d, (e) S 2p and (f) survey spectrum.

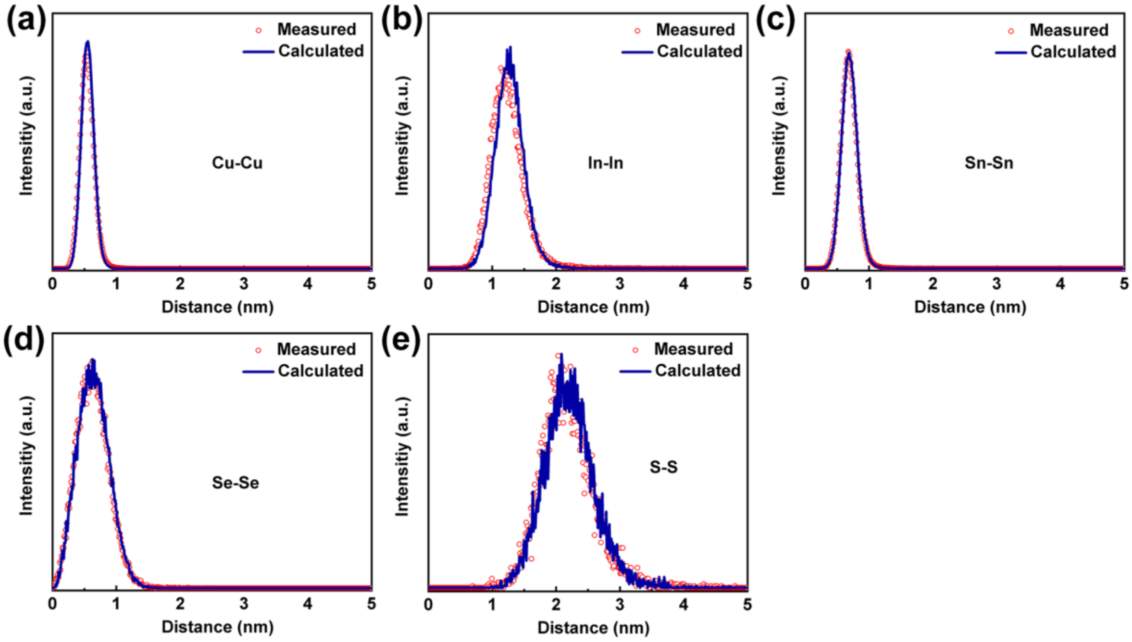

Fig. S14 Nearest-neighbor atomic distribution histograms of Cu, In, Sn, Se, S for SPSed-$Cu_2In_{0.09}Sn_{0.91}Se_2S$. The navy-blue line represents the calculated curves assuming all elements are homogeneously and randomly distributed in the material.

3. Electronic and phononic band structures

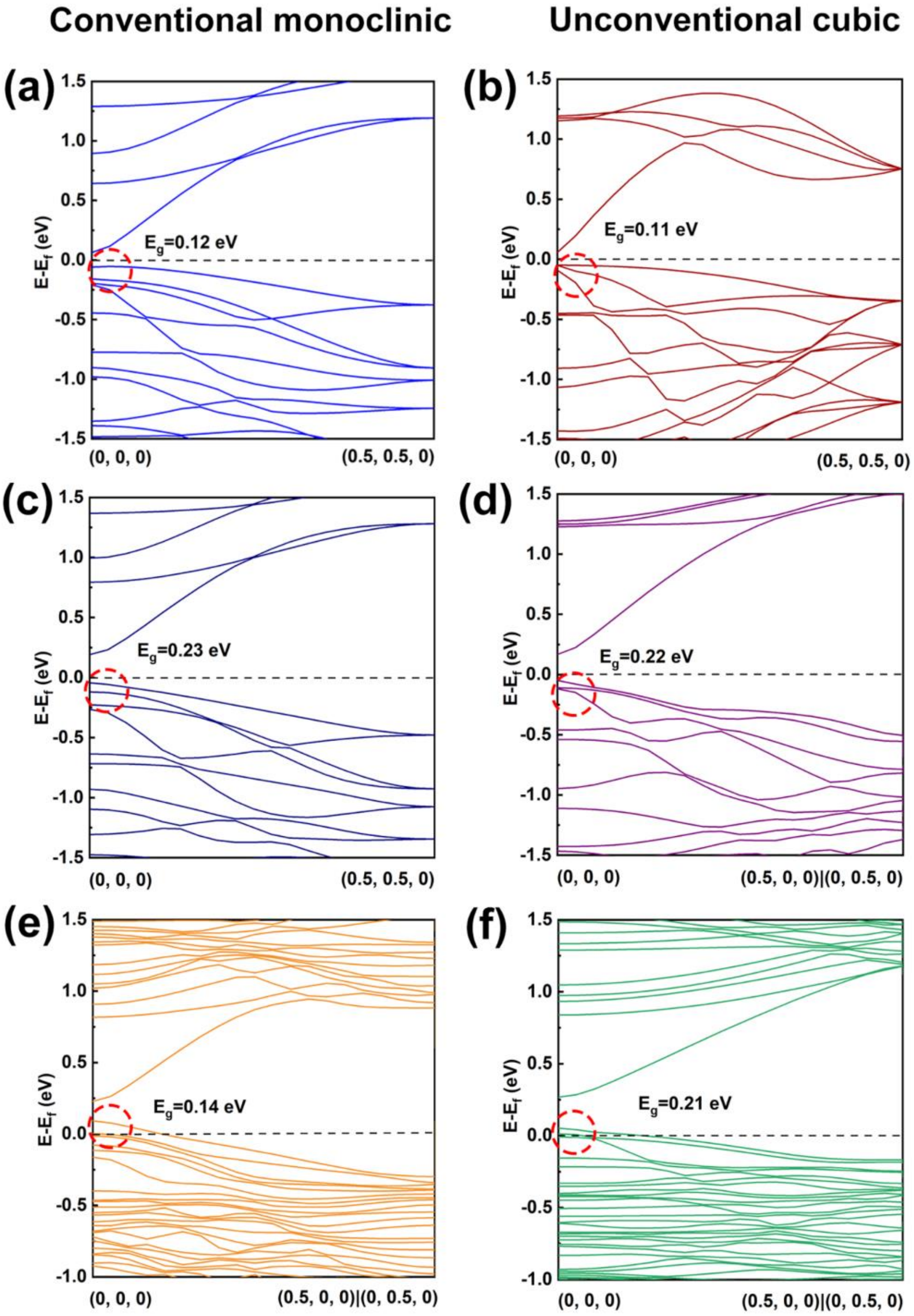

Fig. S15 The electronic energy band structures for (a) monoclinic Cu_2SnSe_3, (b) cubic Cu_2SnSe_3, (c) monoclinic Cu_2SnSe_2S, (d) cubic Cu_2SnSe_2S, (e) monoclinic $Cu_2In_{0.06}Sn_{0.94}Se_2S$ and (f) cubic $Cu_2In_{0.06}Sn_{0.94}Se_2S$.

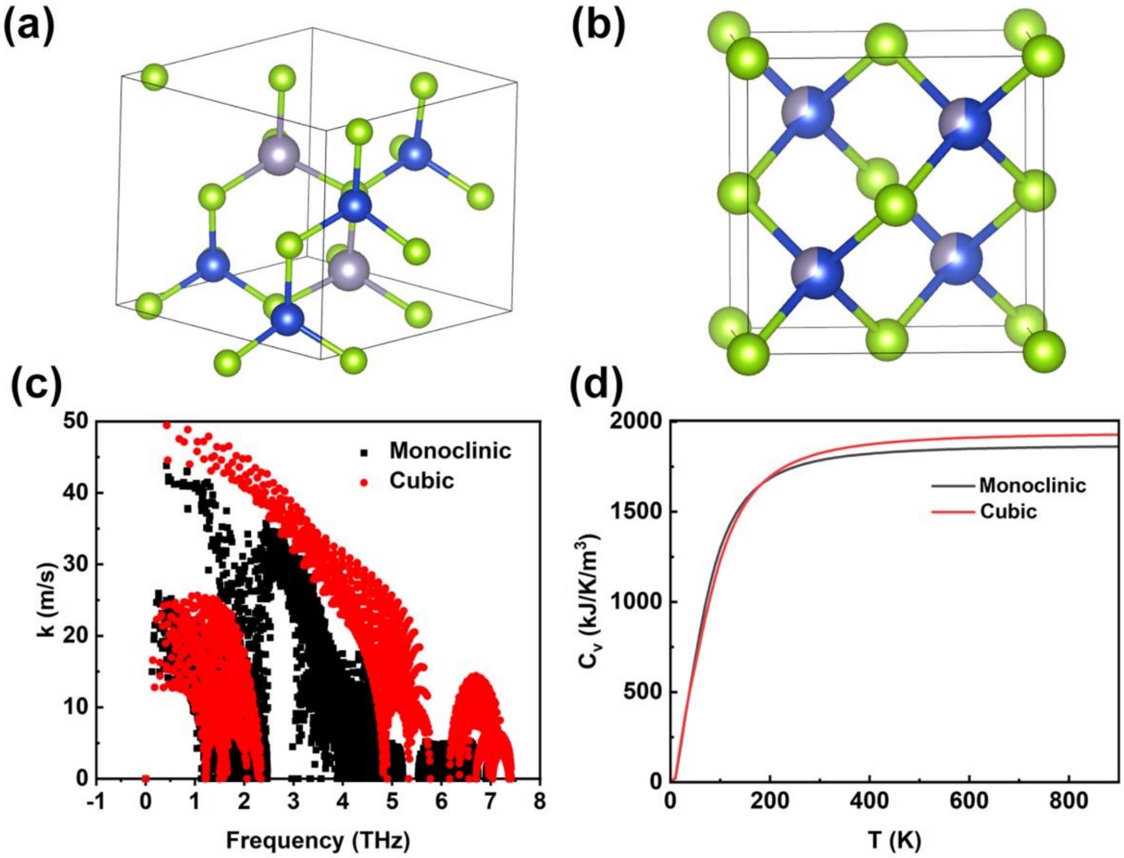

Fig. S16 The crystal structures of (a) monoclinic and (b) cubic Cu_2SnSe_3. (c) The phonon group velocity comparison and (d) the phonon heat capacity comparison between monoclinic and cubic Cu_2SnSe_3.

4. Thermoelectric properties

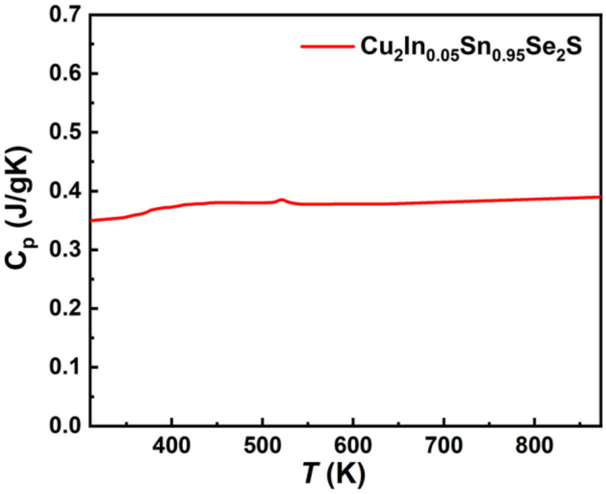

Fig. S17 Temperature dependence of specific heat capacity C_p for SPSed-$Cu_2In_{0.05}Sn_{0.95}Se_2S$.

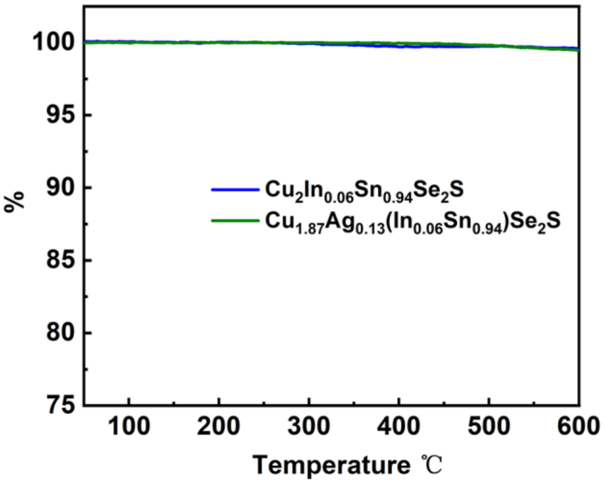

Fig. S18 Thermal gravimetric analysis (TGA) of SPSed-$Cu_2In_{0.06}Sn_{0.94}Se_2S$ and SPSed-$Cu_{1.87}Ag_{0.13}(In_{0.06}Sn_{0.94})Se_2S$ from 50 °C to 600 °C with nitrogen protection. The weight losses of both samples are less than 1%.

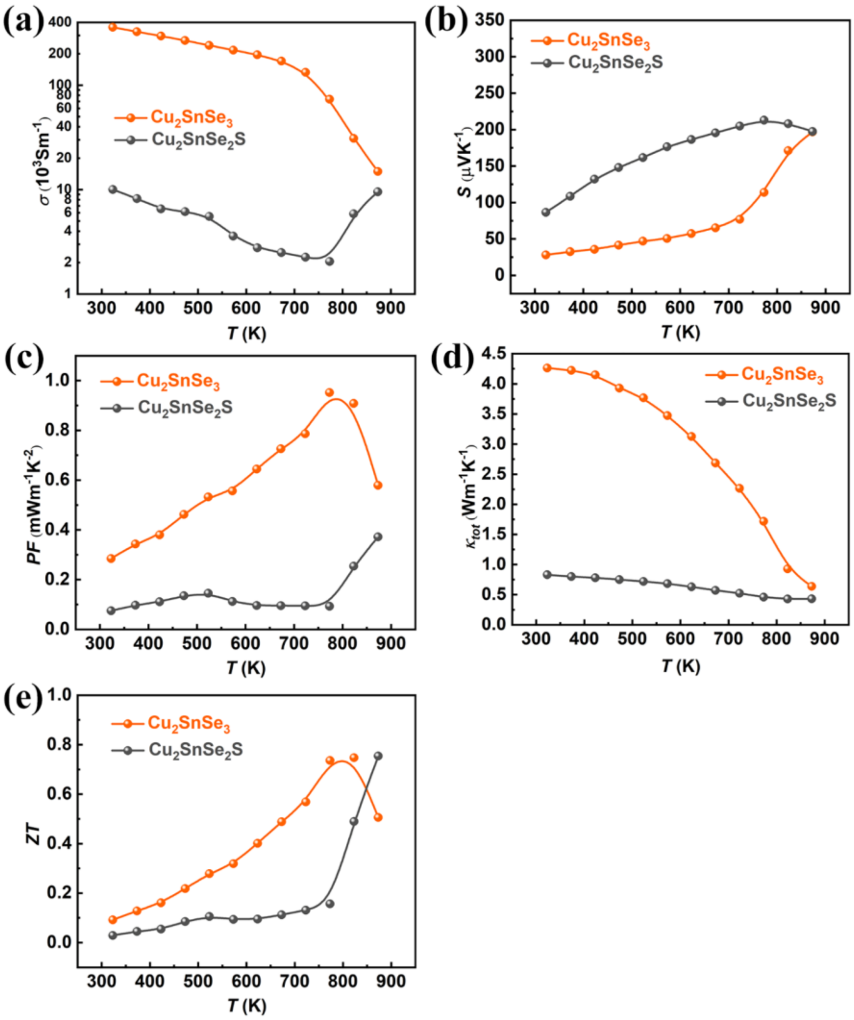

Fig. S19 Temperature dependence of (a) electrical conductivity σ; (b) Seebeck coefficient *S*, (c) power factor *PF*, (d) total thermal conductivity κ_{tot} and (e) *ZT* values for Cu_2SnSe_3 and Cu_2SnSe_2S.

Fig. S20 shows the thermoelectric properties of $Cu_2In_{0.02}Sn_{0.98}Se_2S$, $Cu_2In_{0.14}Sn_{0.86}Se_2S$, $Cu_2In_{0.4}Sn_{0.6}Se_2S$ and $Cu_3InSnSe_3S_2$ in the temperature range of 323-873 K. It is found that with a large increase of In content, the electrical conductivity σ decreases sharply (Fig. S20a) and the S value increases (Fig. S20b). Specifically, σ decreases from 7.89×10^3 S m^{-1} for $Cu_2In_{0.02}Sn_{0.98}Se_2S$ to 1.38×10^3 S m^{-1} for $Cu_3InSnSe_3S_2$ at 873 K, S increases from 225.38 μV K^{-1} for $Cu_2In_{0.02}Sn_{0.98}Se_2S$ to 288.84 μV K^{-1} for $Cu_3InSnSe_3S_2$ at 873 K. Despite the enhanced Seebeck coefficient, the power factor (PF) of $Cu_3InSnSe_3S_2$ (0.11 mW m^{-1} K^{-2} at 873 K) is smaller than that of $Cu_2In_{0.02}Sn_{0.98}Se_2S$ (0.40 mW m^{-1} K^{-2} at 873 K) (Fig. S20c) because of the lower electrical conductivity. Although the thermal conductivity decreases with the increase of In content, the ZT value of $Cu_3InSnSe_3S_2$ sample is not increased.

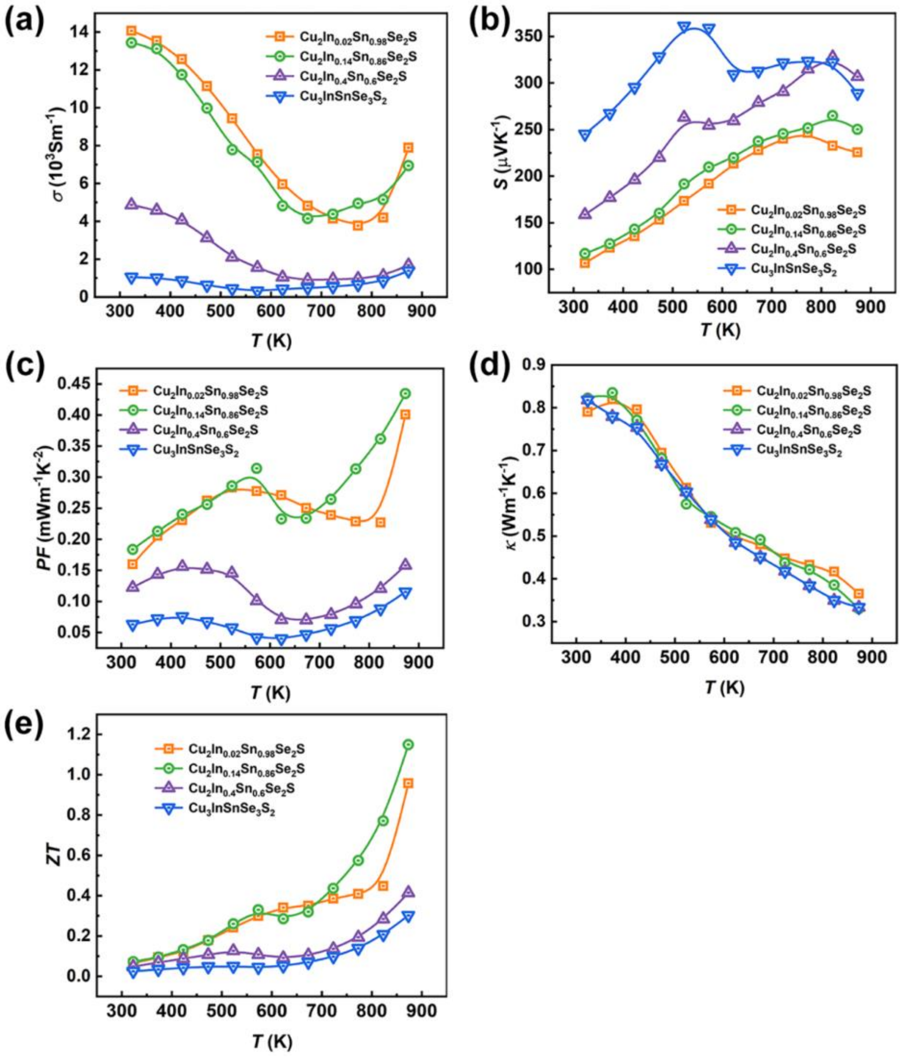

Fig. S20 Temperature dependence of (a) electrical conductivity σ; (b) Seebeck coefficient S, (c) power factor PF, (d) total thermal conductivity κ_{tot} and (e) ZT values for $Cu_2In_{0.02}Sn_{0.98}Se_2S$, $Cu_2In_{0.14}Sn_{0.86}Se_2S$, $Cu_2In_{0.4}Sn_{0.6}Se_2S$ and $Cu_3InSnSe_3S_2$.

The weighted mobility μ_w of $Cu_{2-y}Ag_y(In_xSn_{1-x})Se_2S$ (x= 0, 0.05, 0.06, 0.25, y= 0, 0.07, 0.13) was calculated from the measured electrical conductivity σ and Seebeck coefficient S according to the formula $\mu_w = 331\frac{cm^2}{V_s}\left(\frac{m\Omega\, cm}{\rho}\right)\left(\frac{T}{300\,K}\right)^{-\frac{3}{2}}[\frac{\exp\left[\frac{|S|}{k_B}-2\right]}{1+\exp\left[-5\left(\frac{|S|}{\frac{k_B}{e}}-1\right)\right]}+\frac{\frac{3}{\pi^2}\frac{|S|}{k_B/e}}{1+\exp\,[5(\frac{|S|}{\frac{k_B}{e}}-1)]}]$.[17] As shown in Fig. S21a, the weighted mobility of the samples is not high and decreases with temperature before 723 K because of phonon scattering. The enhancement on μ_w is especially significant near room temperature as the In doping and when the temperature reaches 773 K, the weighted mobility μ_w of $Cu_{2-y}Ag_y(In_xSn_{1-x})Se_2S$ (x= 0, 0.05, 0.06, 0.25, y= 0, 0.07, 0.13) is improved. Benefitting from the improved μ_w values, as well as the decreasing value of κ_L, the ZT value was enhanced after In-doping and Ag-alloying, which can be confirmed by the enhancement of thermoelectric quality factor B via doping In and alloying Ag (Fig. S21b). The quality factor B is designed to estimate the optimal thermoelectric performance for specified materials and proportional to the weighted mobility divided by the lattice thermal conductivity μ_w/κ_L according to the formula $B = (\frac{k_B}{e})^2\,\frac{8\pi e(2m_e k_B T)^{3/2}}{3h^3}\cdot\frac{\mu_w}{k_L}T$.[17]

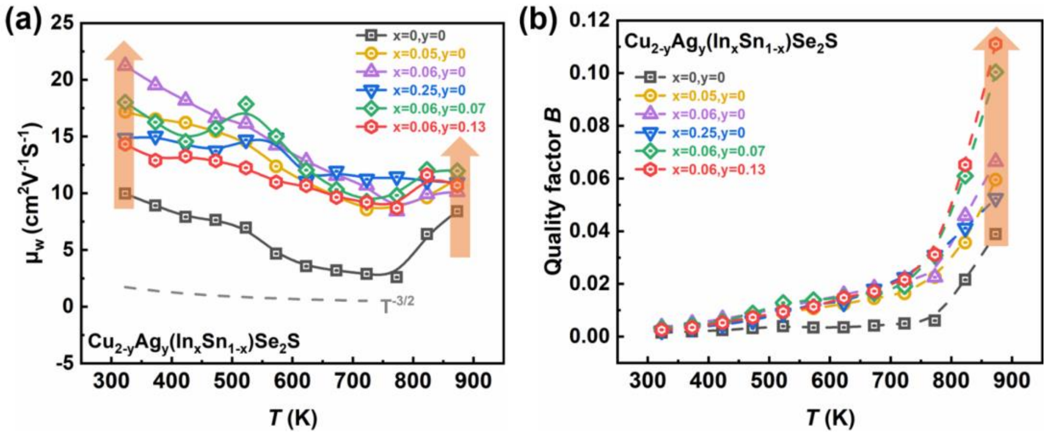

Fig. S21 (a) The weighted mobility μ_w and (b) Quality factor B as a function of temperature of $Cu_{2-y}Ag_y(In_xSn_{1-x})Se_2S$ (x= 0, 0.05, 0.06, 0.25, y= 0, 0.07, 0.13) samples.

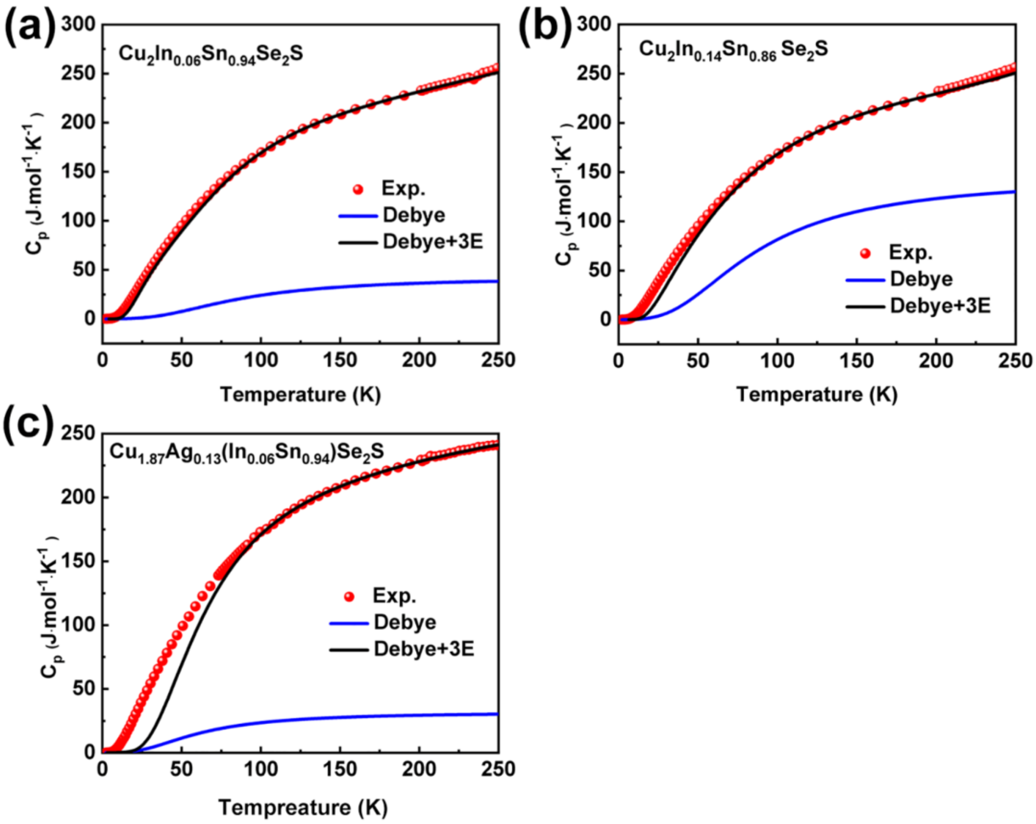

Fig. S22 The experimental C_p with respect to T at low temperature fitted by a combination of Debye and three Einstein models. Red dots illustrate the experimental heat capacity plotted as C_p versus T for (a) SPSed-$Cu_2In_{0.06}Sn_{0.94}Se_2S$, (b) SPSed-$Cu_2In_{0.14}Sn_{0.86}Se_2S$ and (c) SPSed-$Cu_{1.87}Ag_{0.13}(In_{0.06}Sn_{0.94})Se_2S$. Obviously, the data can be fitted only with the Debye–3 Einstein model rather than the Debye model.

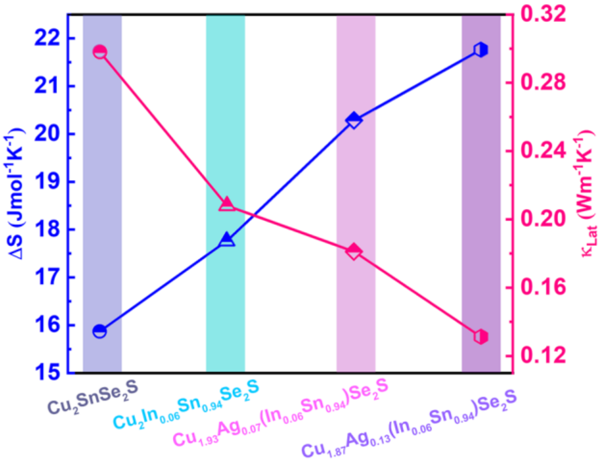

Fig. S23 Calculated configurational entropy ΔS and lattice thermal conductivities (κ_{Lat}) for Cu_2SnSe_2S, $Cu_2In_{0.06}Sn_{0.94}Se_2S$, $Cu_{1.93}Ag_{0.07}(In_{0.06}Sn_{0.94})Se_2S$ and $Cu_{1.87}Ag_{0.13}(In_{0.06}Sn_{0.94})Se_2S$.

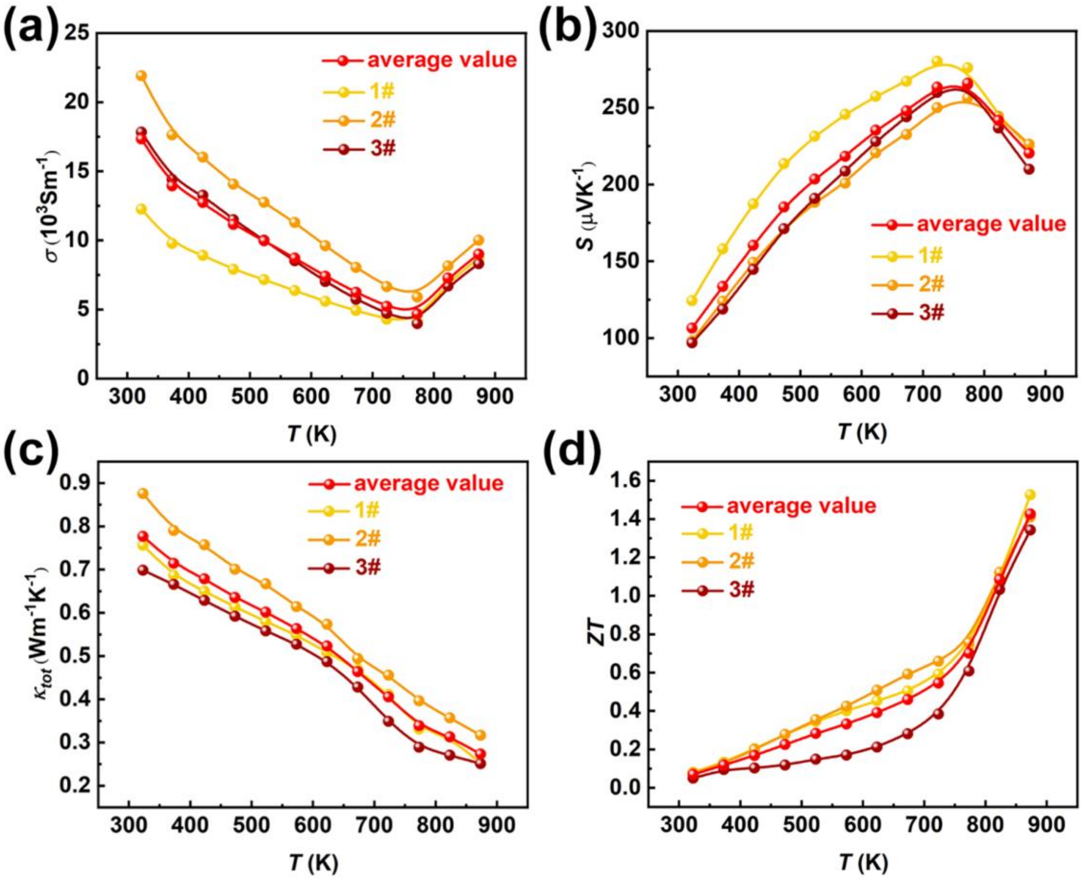

Fig. S24 Data repeatability of (a) electrical conductivity σ, (b) Seebeck coefficient *S*, (c) total thermal conductivity κ_{tot} and (d) *ZT* values for $Cu_{1.87}Ag_{0.13}(In_{0.06}Sn_{0.94})Se_2S$.

Table S4. Fitting parameters for modelling C_p vs. *T* plot given in Fig. S18 in the main text.

Parameter	
θ_{E1} (K)	305.94 K
θ_{E2} (K)	4.02 K
θ_{E3} (K)	100 K
θ_D (K)	359.19 K

Table S5. Comparison between the Present and Literature-Reported Properties of Cu_2SnSe_3-based materials.

Sample description	Synthetic strategy	Phase structure	κ_{Lat} [a] (W / mK)	μ_H [a] ($cm^2 V^{-1} s^{-1}$)	$(\mu_H / \kappa_{Lat})\cdot(m_d^*/m_e)^{3/2}$ [a] ($10^{-3} m^3 KV^{-1} s^{-1} W^{-1}$)	ZT [a]
this work, $Cu_2In_{0.06}Sn_{0.94}Se_2S$	colloidal synthesis	cubic	0.68	1.75	0.21	0.07
Ming, $Cu_2Sn_{0.82}In_{0.18}Se_{2.7}S_{0.3}$ [18]	melting	monoclinic	1.32	7.80	0.26	0.04
Li, $Cu_{1.85}Ag_{0.15}Sn_{0.9}In_{0.1}Se_3$ [13]	ball milling	monoclinic	1.30[b]	5.23	0.17	0.06

[a] All the values are measured at ~300 K. [b] Calculated from $\kappa_{Lat} = \kappa_{tot} - \kappa_e$.

References in the supporting information

1. X. Qiu, J. W. Thompson and S. J. L. Billinge, *J. Appl. Crystallogr.*, 2004, **37**, 678.

2. C. L. Farrow, P. Juhas, J. W. Liu, D. Bryndin, E. S. Božin, J. Bloch, T. Proffen and S. J. L. Billinge, *J. Phys.: Condens. Matter.*, 2007, **19**, 335219.

3. G. Kresse and J. Furthmüller, *Phys. Rev. B.*, 1996, **54**, 11169-11186.

4. S. L. Dudarev, G. A. Botton, S. Y. Savrasov, C. J. Humphreys and A. P. Sutton, *Phys. Rev. B.*, 1998, **57**, 1505-1509.

5. A. Togo and I. Tanaka, *Scr. Mater.*, 2015, **108**, 1-5.

6. S. Kirklin, J. E. Saal, B. Meredig, A. Thompson, J. W. Doak, M. Aykol, S. Rühl and C. Wolverton, *npj Comput. Mater.*, 2015, **1**, 15010.

7. L.-D. Zhao, G. Tan, S. Hao, J. He, Y. Pei, H. Chi, H. Wang, S. Gong, H. Xu, V. P. Dravid, C. Uher, G. J. Snyder, C. Wolverton and M. G. Kanatzidis, *Science*, 2016, **351**, 141-144.

8. M. K. Jana, K. Pal, A. Warankar, P. Mandal, U. V. Waghmare and K. Biswas, *J. Am. Chem. Soc.*, 2017, **139**, 4350-4353.

9. B. Koley, A. Lakshan, P. R. Raghuvanshi, C. Singh, A. Bhattacharya and P. P. Jana, *Angew. Chem. Int. Ed.*, 2021, **60**, 9106-9113.

10. J. L. Baker, J. T. White, A. Chen, T. Ulrich, R. R. Roback and H. Xu, *J. Nucl. Mater.*, 2021, **557**, 153282.

11. Y. Lou, W. Zhao, C. Li, H. Huang, T. Bai, C. Chen, C. Liang, Z. Shi, D. Zhang, X.-B. Chen and S. Feng, *ACS Appl. Mater. Interfaces.*, 2017, **9**, 18046-18053.

12. Y. Cui, G. Wang and D. Pan, *CrystEngComm*, 2013, **15**, 10459-10463.

13. Y. Li, G. Liu, T. Cao, L. Liu, J. Li, K. Chen, L. Li, Y. Han and M. Zhou, *Adv. Funct. Mater.*, 2016, **26**, 6025-6032.

14. H. Zhang, T. Ouyang, J. Li, M. Mu and X. Yin, *Electrochim. Acta.*, 2021, **390**, 138766.

15. L. Tan, Z.-Q. Liu, N. Li, J.-Y. Zhang, L. Zhang and S. Chen, *Electrochim. Acta.*, 2016, **213**, 283-290.

16. C.-T. Yang, H.-I. Hsiang and J.-H. Tu, *Adv. Powder Technol.*, 2016, **27**, 959-963.

17. G. J. Snyder, A. H. Snyder, M. Wood, R. Gurunathan, B. H. Snyder and C. Niu, *Adv. Mater.*, 2020, **32**, 2001537.

18. H. Ming, G. Zhu, C. Zhu, X. Qin, T. Chen, J. Zhang, D. Li, H. Xin and B. Jabar, *ACS Nano*, 2021, **15**, 10532-10541.